

Rapid Fabrication of 3D Chiral Microstructures by Single Exposure of Interfered Femtosecond Vortex Beams and Capillary-Force-Assisted Self-Assembly

Deng Pan, Shunli Liu, Jiawen Li,* Jincheng Ni, Chen Xin, Shengyun Ji, Zhaoxin Lao, Chenchu Zhang, Bing Xu, Rui Li, Shengyin Fan, Pengju Li, Yanlei Hu, Dong Wu,* and Jiaru Chu

The rapid fabrication of 3D chiral microstructures is of great significance in the fields of optics and mechanics. Here, a hybrid strategy is presented that combines spatial-light-modulator-assisted two-photon polymerization (SATPP, top-down) and capillary-force-assisted self-assembly (bottom-up) for efficiently yielding chiral microstructures. Based on SATPP, the pre-subunit can be efficiently fabricated via 3D chiral discrete vortex beam (CDVB), which is generated by interfering multiple parallel vortex beams. Then, the 3D chiral microstructures are assembled by subunits with the aid of meniscus-directed capillary force. This strategy can fabricate stable 3D chiral microstructures and improve the manufacturing efficiency by more than 100 times. Furthermore, the height, diameter, rotation angle, and handedness of chiral microstructure can be flexibly regulated. Because the obvious chiral feature of the manufactured assembly, it can exhibit strong vortical dichroism when excited by the light carrying orbital angular momentums. Also, it can be used to prepare functional microrobots base on the chiral body rotation. This hybrid strategy can rapidly manufacture 3D chiral microstructures, which can be utilized as multifunctional scalable platform with promising prospect in micro/nano robotics, optical sensors, and advanced functional devices.

interaction with light,^[2] because The 3D configuration of microstructures can greatly enhance the optical response.^[3] However, these strategies for fabricating 3D chiral microstructures are not scalable and most of them are complex, expensive, and time-consuming, which limits their further potential applications. As a promising top-down micro/nano-fabrication strategy with high processing resolution, two-photon polymerization (TPP) can fabricate true 3D microstructures via point-by-point femtosecond laser beam scanning, which has been widely used in microoptics, microfluidic, micro-mechanics and life sciences.^[4] However, the traditional point-by-point scanning strategy needs a lot of fabrication time.^[5] For improving the TPP efficiency, the spatial-light-modulator-assisted femtosecond laser two-photon polymerization (SATPP) came into being. This strategy uses shaped femtosecond laser beam to expose photoresist for obtaining microstructures,


which has been widely used in the fabrication of patterned and functional microstructures such as microtubes, micropillars, and microcages.^[6] Theoretically, by modulating the wavefront, the femtosecond laser beam can be flexibly adjusted to arbitrary shape for the single exposure fabrication of 3D microstructures.^[7] Although many outstanding works have been reported in the fabrication of 3D chiral microstructures with SATPP,

1. Introduction

Chiral structures, such as plant vines, spirochetes, and drug molecules, are widespread and essential in nature.^[1] Recent studies have proved that the chiral microstructures, especially 3D microstructures, are of great significance in the field of optics sensing and optics detection due to their nontrivial

D. Pan, S. Liu, J. Li, C. Xin, S. Ji, R. Li, S. Fan, P. Li, Y. Hu, D. Wu, J. Chu
Hefei National Laboratory for Physical Sciences at the Microscale
CAS Key Laboratory of Mechanical Behavior and Design of Materials
Department of Precision Machinery and Precision Instrumentation
University of Science and Technology of China
Hefei, Anhui 230027, China
E-mail: jwl@ustc.edu.cn; dongwu@ustc.edu.cn

J. Ni
Department of Electrical and Computer Engineering
National University of Singapore
Singapore 117583, Singapore

 The ORCID identification number(s) for the author(s) of this article can be found under <https://doi.org/10.1002/adfm.202106917>.

Z. Lao
School of Instrument Science and Opto-electronics Engineering
Hefei University of Technology
Hefei 230009, China

C. Zhang
Anhui Province Key Lab of Aerospace Structural Parts Forming
Technology and Equipment
Institute of Industry & Equipment Technology
Hefei 230009, China

B. Xu
School of Mechanical Engineering
Suzhou University of Science and Technology
Suzhou 215009, China

DOI: 10.1002/adfm.202106917

further research progress is still necessary over the aspect of larger chiral beam diameter, more reliable stability, and more abundant applications.

Recent developments of utilizing self-assembly technology offer possible ways for efficiently fabricating 3D chiral microstructures.^[8] For example, the synthesis of precise molecules-like microstructure was firstly proved by D. Zerrouki et al. via a colloidal self-assembly strategy, which can self-assemble colloids into various controlled chiral clusters.^[9] Furthermore, the programmable self-assembly of micron-sized colloidal clusters with prescribed binding angles, dihedral angles, and chiralities was realized by Ben Zion et al. They combined DNA nanotechnology with colloidal science, offering intriguing possibilities for building large-scale intricate and functional structures.^[10] As a bottom-up fabrication strategy, the self-assembly can prepare and regulate the morphologies of the complex micro/nano structures by assembling pre-existing components into an organized structure in a bottom-up manner. Especially, capillary force assisted self-assembly (CFAS) has attracted great attention due to many advantages including low cost, simplicity, and scalability.^[11] Pokroy et al. used the two-step soft transfer of a silicon template to prepare chiral hierarchical helical arrays with uniform, periodic patterns by CFAS.^[12] Because the capillary force is difficult to harness at the microscale, this strategy lacks of robustness and cannot control the handedness of chiral arrays. In order to utilize capillary force for inducing chiral structures to assemble on a microscopic scale, a feasible method is to pre-design the shape of subunits to guide the direction of capillary force and form a stable chiral 3D microstructure.

In this work, we proposed a hybrid strategy of fabricating chiral microstructures by the combination of SATPP (top-down) and CAFS (bottom-up). A method called off-axial interference is adopted for generating the 3D chiral discrete vortex beam (CDVB), in which multiple parallel vortex beams in different axis are interfered and focused by an oil-immersed high numerical aperture (NA) objective lens. Fresnel diffraction and Debye diffraction are used to calculate the light intensity distribution of the CDVB in free space and tight focusing conditions, respectively. By the CDVB single exposure, a subunit can be efficiently fabricated within 0.5 seconds, which can improve the fabrication efficiency by 102 times. Besides, we introduce the CFAS and firstly combine it with SATPP to assemble these subunits into stable 3D chiral microstructures. The height, diameter, rotation angle, and handedness of the 3D chiral microstructures can be flexibly adjusted by changing the parameters of CDVB. The dynamical assembly process is observed for studying the assembly modes under different parameters. In addition, the driving force/physical mechanism of chirality emergence is proposed based on the force analysis and verified by numerical simulation methods. It is worth noting that the prepared 3D chiral microstructures have good stability and can remain stable after many soaking-drying circles. Besides, it can be found that the 3D chiral microstructures exhibit strong vortex dichroism when excited by the light carrying orbital angular momentums (OAM), which shows potential application in optics sensing. Finally, the 3D chiral microstructures can be used to prepare the functional microrobots with various heads (cylindrical, cone-shaped, and phage-shaped) for the controllable movements. This hybrid strategy can prepare

chiral microstructures efficiently and economically, which has promising prospects in the fields of micro/nano robots, optical sensing, advanced photonic devices, and etc.

2. Results and Discussion

2.1. Generation of 3D Chiral Discrete Vortex Beams (CDVB)

Optical vortex with integer topological charge n can carry a quantized OAM $n\hbar$ per photon (where \hbar is reduced Planck constant, $\hbar/2\pi$),^[13] which has been widely used in the fields of quantum communication, particle manipulation, and high resolution imaging.^[14] A vortex beam with a helical phase wavefront can be expressed as $u = \exp(in\theta)$, where n is the topological charge number. Although the vortex beam carries chiral OAM information, it shows an achiral “donuts”-shaped light intensity distribution in space. Here, we find that the off-axial interference of vortex beams can break the annular intensity distribution of vortex beam and generate the 3D structural beam with a helical focus. Compared with coaxial interference, this method can generate 3D chiral light field with a wider range of adjustable beam diameter and richer morphologies (Figures S1 and Figure S2, Supporting Information).^[15] The topological charges are spatially distributed and the total phase of the CDVB can be written as

$$\varphi = \arg \left[\prod_{i=1}^N (u - m_i)^{n_i} \right] \quad (1)$$

where the m_i and n_i are the complex position and value of the i -th topological charge. Hence the total topological charge $Q = \sum_i n_i$ can be calculated by summing over all the topological charges. The hologram is generated by the commercial software MATLAB, and the detailed generation process can be seen in the Experimental Section. Here, Fresnel diffraction is used to show the light intensity distribution of vortex beam and CDVB, which is

$$U(x, y) = -i/\lambda \iint U_0(x_0, y_0) \times \exp(ikr)/r \times \cos\theta dx_0 dy_0 \quad (2)$$

and the double Fourier transform method is used here to simplify the calculation, which is written as

$$U(x, y) = FFT^{-1} \{ FFT \{ U_0(x_0, y_0) \} \exp\{ jkd[1 - \lambda^2(u^2 + v^2)/2] \} \} \quad (3)$$

where the U and U_0 are the complex amplitude distribution of observation plane and diffraction plane. According to the simulation results, a common vortex beam propagates in the form of annular intensity distribution in the free space (Figure 1a). When several parallel vortex beams interfere, the CDVB is formed, resulting in a variety of interference patterns. For example, when the centers of the three interferential vortex beams are not concentric but collinear, the diffracted light intensity distribution retains partial annular characteristics of the vortex beam and becomes elliptical (Figure S3, Supporting Information). When the centers of the three interferential

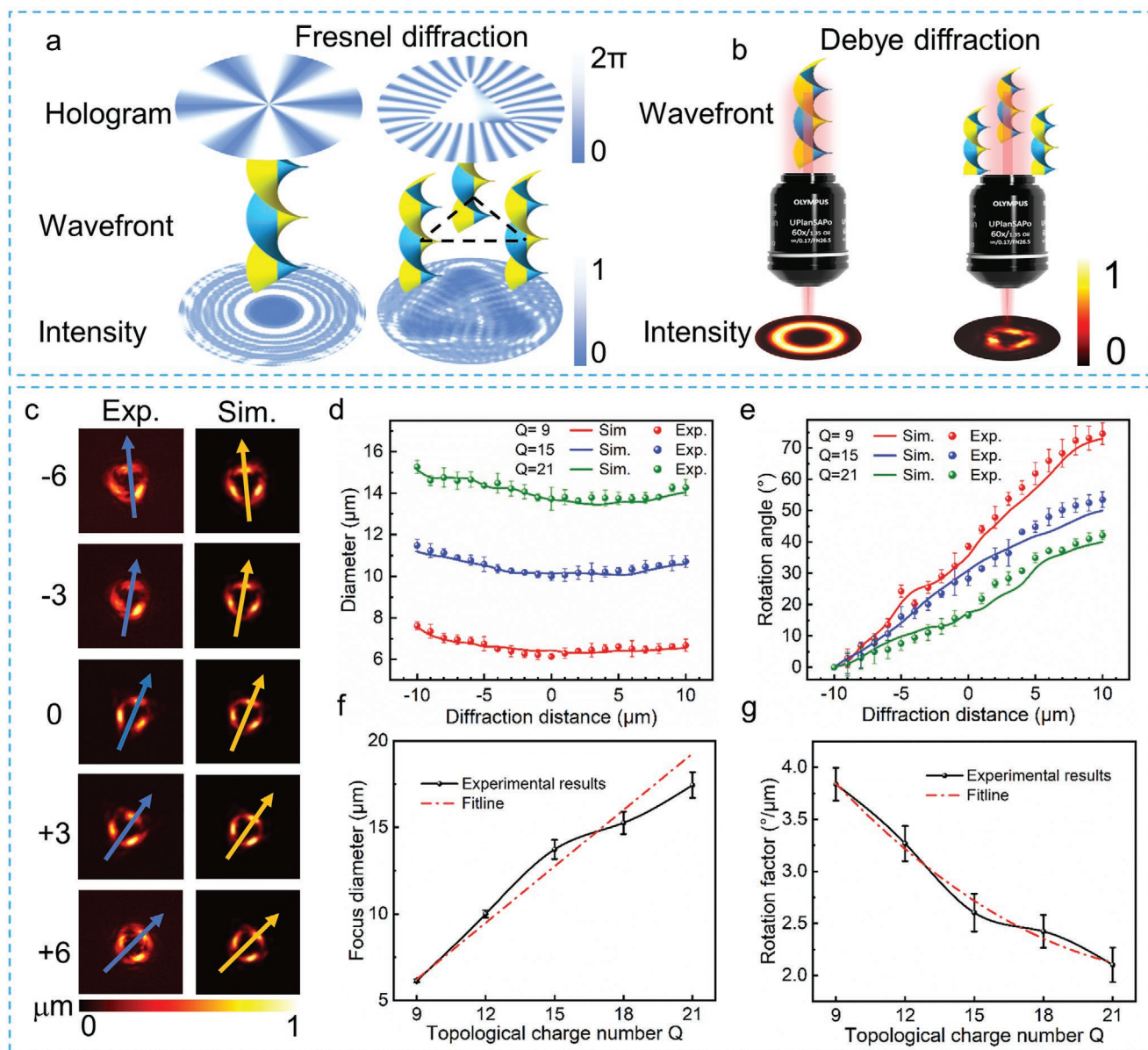


Figure 1. Generation of CDVB by off-axis interference of multiple vortex beams. a) Optical holograms, phase wavefronts, and intensity distributions of vortex and CDVB in free space. b) Single vortex beam and off-axis non-collinear interfering vortex beam are focused by a high NA objective lens. c) Simulated and experimental intensity profiles of the CDVB from diffraction distance $-6 \mu\text{m}$ to $+6 \mu\text{m}$ under a high NA objective lens. d) Quantitative relationship between diameter, e) rotation angle of the CDVB and diffraction distance with topological charge number $Q = 9, 15, 20$, respectively. The f) diameter on the focal plane and the g) rotation factor ($^\circ \mu\text{m}^{-1}$) along the optical axis of CDVB are functions of Q , respectively.

vortex beams are at the vertices of a triangle, the continuous “donuts”-shaped intensity distribution of a single vortex beam is completely destroyed and replaced by a discrete and centrosymmetric intensity distribution as expected. In a conventional TPP system, the laser beam is focused by a high NA objective lens which leads to a tight focusing mode. When a common vortex beam is tightly focused, a ring-shaped light intensity distribution is generated. While for the CDVB, a bright and discrete petal-like spot can be clearly observed, which inherits the CDVB’s discrete helical wave front (Figure 1b).

The Debye diffraction calculation is realized by the commercial software MATLAB for simulating the CDVB intensity

distribution under the oil-immersed objective lens. The Debye diffraction integral formula can be written as

$$\bar{U} = -iC/\lambda \iint [\bar{U}_r \times \exp(ik_z z)/\cos\theta] \times \exp[-i(k_x x + k_y y)] kr dk_x k_y \quad (4)$$

and it can be rewritten in the form of Fourier transform, which is

$$\bar{U}(x, y, z) = -iC/\lambda \text{FFT}[\bar{U}_r \times \exp(ik_z z)/\cos\theta] \quad (5)$$

The simulation and experiment results of the vector CDVB intensity distribution from $-6 \mu\text{m}$ to $+6 \mu\text{m}$ are shown in

Figure 1c, Video S1, where the arrow indicates a specified direction in order to show the rotation of CDVB clearly. During the propagation, the multi-petal spot rotates while its diameter is almost unchanged (Figure 1d), which is attributed to tight focus mode and the discrete helical wavefront of CDVB. Figure S4 in the Supporting Information shows numerical simulations of the CDVB with three and four lobes, revealing that the CDVB exhibits a patterned light intensity distribution and a rotating wavefront. Moreover, the parameters of CDVB such as diameter and rotation angle depend on the total topological charge Q . On the one hand, the diameter of CDVB can be regulated by the total topological charge Q , and a greater Q generates a larger diameter. As shown in Figure 1f, as the Q increases from 9 to 21, the focus diameter of the CDVB increases from 7 μm to 17 μm . Besides, the diameter of CDVB can also be affected by the center distance of the multiple vortex beams, which is shown in Figure S5 in the Supporting Information. However, when adjusting the beam diameter by changing center distance, the adjustment range is limited. Therefore, we adopt the method of changing Q to adjust the CDVB's diameter. On the other hand, the rotation angle can also be regulated by Q , and a smaller Q leads to a bigger CDVB rotating trend, as shown in Figure 1e. Here, rotation factor is defined as the rotation angle per micrometer. It can be found that as the topological charge Q increases from 9 to 21, the rotation factor decreases from 3.8 to 2.1° μm^{-1} (Figure 1g).

2.2. Fabrication of Subunits by Single Exposure of CDVB

For single exposing 3D microstructures with CDVB, a spatial-light-modulator-assisted TPP system is adopted as shown in Figure 2a. The power of femtosecond laser (Chameleon Vision-S, Coherent Inc, a repetition rate of 80MHz, a pulse width of 75 fs) is adjusted by the two polarizers and Glan-Taylor prism, then the laser is expanded by a beam expander and reflected by a spatial light modulator (SLM) (Pluto NIR-2; Holoeye Photonics AG, pixels of 1920 \times 1080, a pixel pitch of 8 μm). After that, the beam is shrunken by a 4f system which consists of two lenses for matching the size of the objective lens pupil. Finally, the CDVB is focused into the photoresist (SZ2080) by the oil-immersed objective lens (NA = 1.35). The hologram loaded on the SLM is a superposition of multiple holograms including the origin phase of CDVB, a singular point mask, and a blazed grating with period T (Figure 2b). The superposition can be expressed by

$$Phase_{sim} = \text{mod}(Phase_{CDVOF} + Phase_{BG} + Phase_{mask}, 2\pi) \quad (6)$$

$$Phase_{BG} = 2\pi \times x/T \quad (7)$$

where “mod” represent the remainder operation, which makes sure that the phase 0 ~ 2 π of phase corresponds to gray value 0 ~ 255 of hologram. It is worth noting that the singular point mask is used to avoid the focusing effect caused by singularity phase, otherwise there will be a strong focus in the center of CDVB (Figures S6 and Figure S7, Supporting Information). The function of the blazed grating is to deflect the CDVB to the first-order beam and separate it from the zero-order beam.

Before the fabrication, the photoresist needs to be heated at 100 °C for 1 hour. After baking, the photoresist is placed under the oil-immersed objective lens and exposed by the CDVB. Then, the sample is immersed in acetone for removing unprocessed area. Finally, the whole sample is dried with a carbon dioxide critical dryer for obtaining the exposed microstructures without capillary influence.

Since the CDVB will rotate when propagating under the objective lens, subunits can be fabricated by single exposure (Video S2), and typical 45° and top view SEM photos of the fabricated subunits are shown in Figure 2c,d. Here, the parameters of the CDVB can be flexibly adjusted, resulting controllable morphologies of the subunits. The diameter (D) and rotation angle (RA) are defined by the max diameter and single-petal rotation angle of subunits measured in the top view SEM photos. In addition, the processing height can also be regulated by controlling the exposure depth, which means that a deeper exposure depth will result in a higher subunit, as shown in Figure 2e,f. Moreover, the diameter of the CDVB changes as it propagates, which causes changes in the diameter of the subunits with varied processing height. To prove this point, quantitative relationship between the diameter of the subunits and the processing height with different topological charges Q is shown in Figure 2g. The diameter of the subunits firstly decreases and then increases as the processing height increases, and its minimum value corresponds to the focus diameter of the CDVB on the focal plane. Figure 2h shows the relationship between the rotation angle of the subunits and the processing height within the processing range. A smaller Q corresponds to a more significant rotation phenomenon, which is consistent with the aforementioned characteristics of the CDVB. The minimum diameter and rotation factor (° μm^{-1}) of subunits with different Q are summarized in Figure S8 in the Supporting Information. Obeying the axial intensity distribution characteristics of the CDVB, an increasing topological charge number Q will lead to a linear increase in minimum diameter and a nonlinear decrease in rotation factor. The 3D microstructures prepared by CDVB single exposure has a sub-micro spatial resolution (Section 3 of supporting information) and are difficult manufactured by the conventional fabrication methods such as lithography and single photon printing due to the axial resolution limitation.^[16]

2.3. Preparation of Chiral Assemblies Assisted by Capillary Force

When the samples are taken out from the developer and directly placed in the air for drying, a concave meniscus is formed inside subunits, resulting in capillary force F_c (Figure S9, Supporting Information). According to the principle of static balance, in order to resist the inward bending tendency caused by the capillary force, the microstructures will yield an internal elastic restoring force F_s at the same time. With a suitable size, the capillary force can construct the discrete three-petal subunits into an integrated chiral assembly. The forming process of the assembly involves complex dynamics principle, which can be clearly observed in the supporting Video S3. To explain the process briefly, optical microscope topographies and schematic

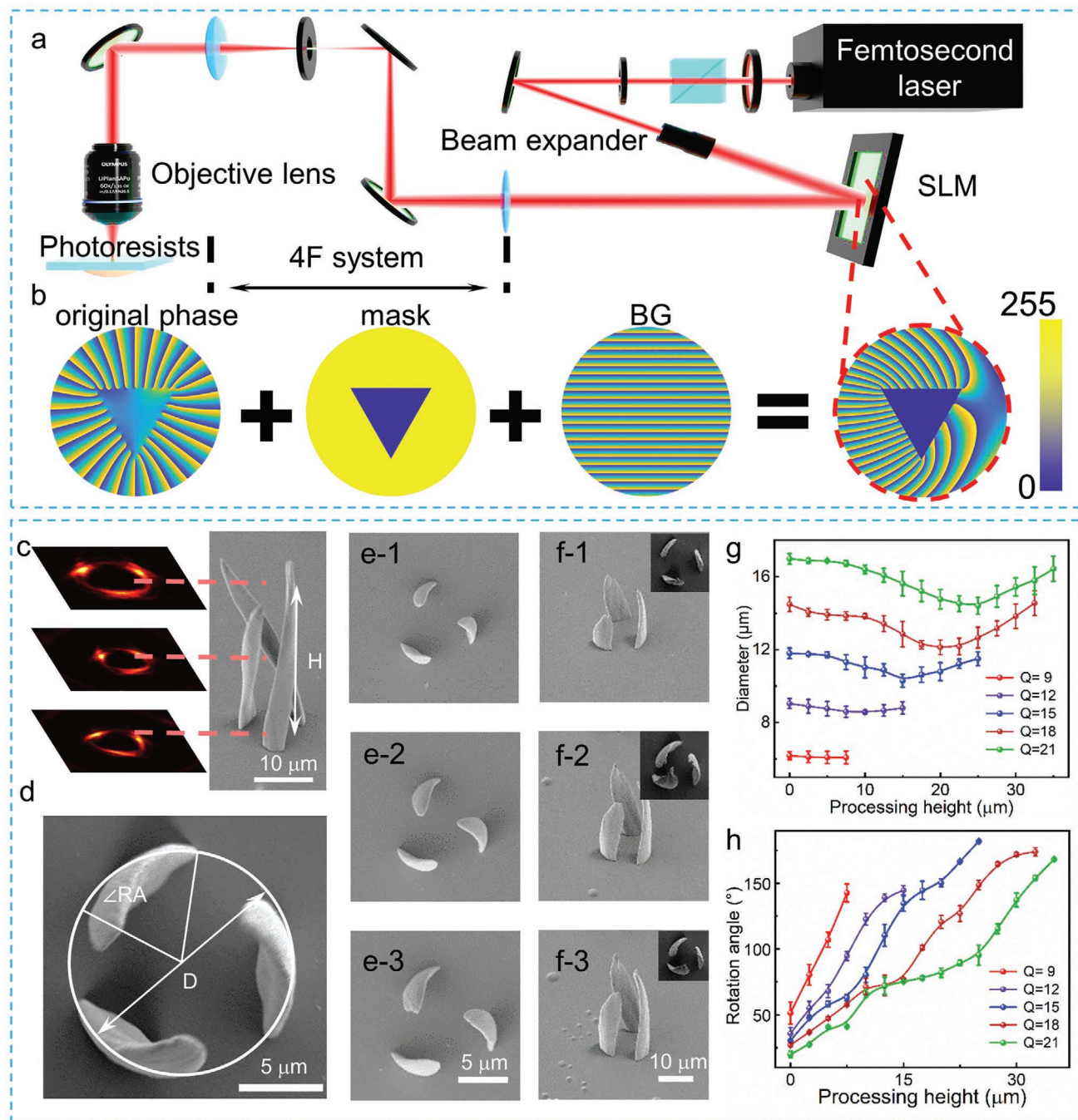


Figure 2. Fabrication of subunits by a single exposure of the CDVB. **a**) The spatial-light-modulator-assisted two-photon polymerization system. **b**) The hologram which is projected onto the SLM is composed of the original phase, mask, and blazed grating. **c**) The subunits and corresponding CDVB. **d**) The top view SEM of subunits. D means the diameter of the subunits measured from the top view, and RA means the rotation angle measure from the bottom to the top of the subunits, **e, f**) The top view and side view of the subunits with increasing diameters and heights. **g**) Quantitative relationship between the diameter of subunits and processing height. **h**) Quantitative relationship between the rotation angle of microstructure and processing height.

diagrams (insets) of the three-helical subunits before, during, and after assembly are demonstrated in **Figure 3a–d**, respectively. The final topography of the three-petal microstructure can be considered as the result of the competition between evaporation-induced capillary force (F_c) and elastic restoring

force (F_s). The capillary force generated by concave meniscus can be described as

$$F_c \sim \frac{h\omega\gamma\cos\theta}{d} \quad (8)$$

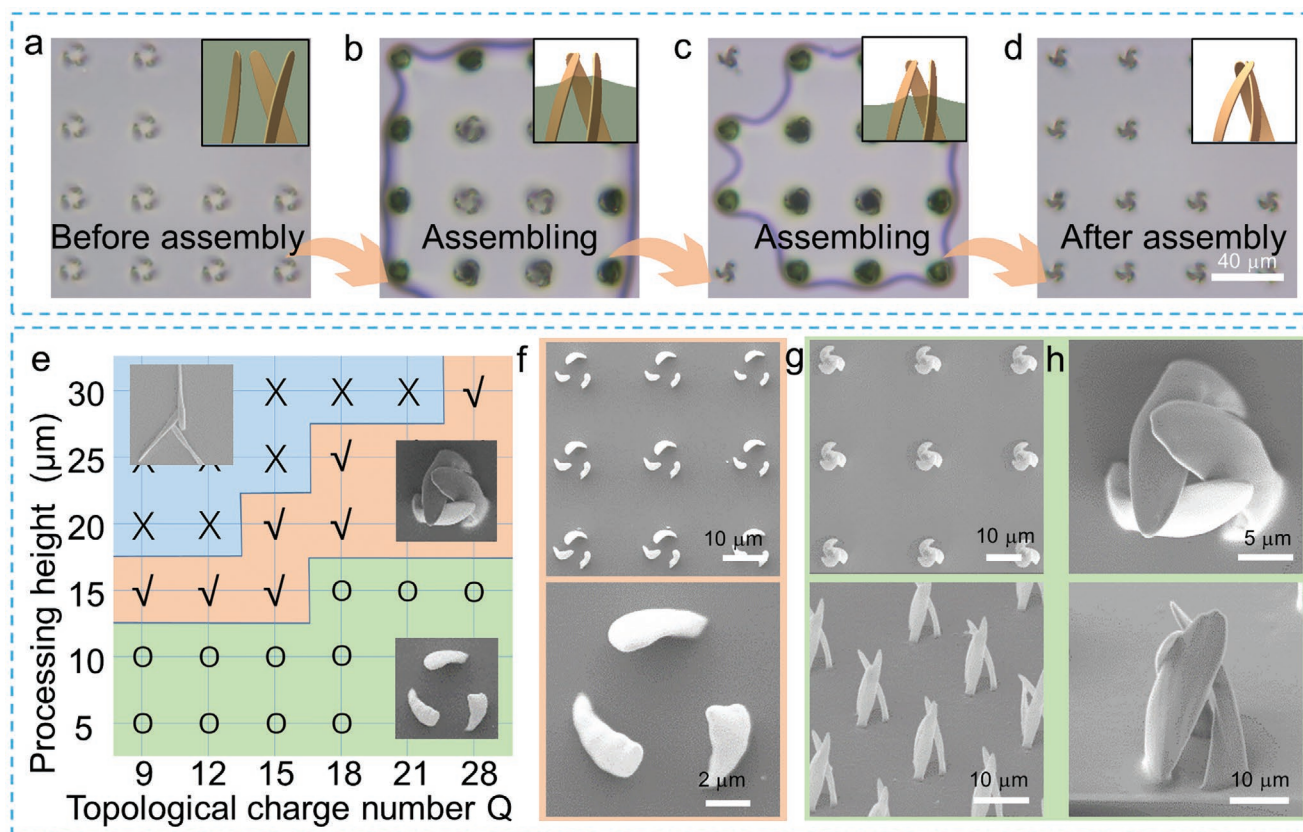


Figure 3. The assembling process and results of the 3D chiral microstructures. a–d) The images of chiral microstructure before assembly, during assembly, and after assembly. e) Phase diagrams summarizing the modes of assemblies. f) Top view of the un-assembled chiral microstructures. g,h) Top view and side view of the assembled chiral microstructure.

in which the F_c is proportional to the interfacial tension γ of the solvent, the height h and the width w of subunits' petal, the cosine of contact angle θ , and inversely proportional to the diameter of the subunits d . And the elastic restoring force can be described as

$$F_s \sim E \frac{t^3 w d}{h^3} \quad (9)$$

where E is the Young's modulus, and t is the thickness of subunits' petal. For a specific exposure microstructure, the relative magnitude of F_c and F_s will determine its final morphology. The detailed discuss about the driving forces and physical mechanism behind the emergence of chirality and control over handedness can be seen in Section 4 of supporting information.

During the assembly process, the maximum capillary force and the maximum elastic restoring force are in the comparable magnitude, the slight changes of the subunits geometry can induce controllable chiral assemblies, which is shown in Figure 3e. The 3D chiral microstructures' morphology driven by liquid capillary force can be divided into three modes: 1. When the height of the subunits is low and $F_c < F_s$, the capillary force is within the limit of the bending resistance. The 3D chiral microstructures still maintain a standing state, corresponding to "O" area in Figure 3e. 2. On the contrary, when the height and diameter of the subunits are within the range of "√"

and $F_c > F_s$, the capillary force exceeds the limit of the bending resistance, and the subunits will form a chiral assemble. 3. The "X" area in Figure 3e indicates the outward tipping due to the excessive height of the subunits.

The controllable morphology and mass manufacture of chiral microstructure can be achieved through the above strategies. Overall and magnified views of discrete mode are shown in Figure 3f. Due to insufficient capillary force, the three petals of each structure are not assembled and still present a discrete state. Based on the discrete mode, appropriately reducing the subunits' diameter or increasing the microstructure height will significantly promote the assembly trend. Finally, stable chiral assembly can be obtained (Figure 3g), which is composed of three discrete petals along a certain direction. Magnified top-view and 45° tilted SEM images of a single assembly for clear observation are shown in Figure 3h. The ordered microarchitecture is artfully constructed by capillary force, thus having a natural curve and an extremely smooth surface. And the tips of the micro petals can adhere to each other in an orderly manner following the rotation of the micro petals, which is difficult to be achieved in other ways. Besides, the height or diameter of the chiral microstructure can be flexibly controlled via controlling the fabrication parameters or beam parameters (Section 5 of supporting information).

This hybrid strategy for preparing the chiral microstructures has the following advantages. 1. It reduces the difficulty of 3D beam shape design and only needs to design some relatively

simple shape light fields to prepare chiral microstructures. 2. Since the chiral microstructures are assembled by subunits, the size of the chiral microstructures can be increased to 10 ~ 30 μm , which is difficult for SATPP directly single exposure fabrication. 3. Compared with the point-to-point scanning method, the strategy that combines self-assembly and SATPP can improve the processing efficiency by 50 to 100 times, which provides the possibility for large-area and mass production. 4. Chiral microstructures are prepared through self-assembly without expensive equipment and complicated steps, which reduces the cost and ensures reliability. Especially, when using the capillary force assisted self-assembly, the chiral microstructures can be assembled only by immersing the sample in the developer and drying in the air, which makes this strategy economical and reach the yield as high as 98.2% (Section 6 of supporting information).

2.4. Fabrication of Variety Morphologies Chiral Assemblies

Various morphologies of the CDVB and assemblies can be obtained by regulating the fabrication parameters. It is obvious that the assemblies have a strong rotation tendency, which reveals the geometric chiral feature. The left-handed, right-handed, discrete and assembled states of the microstructure can be conveniently achieved and arbitrarily combined by changing the parameters of the CDVB, as shown in Figure 4a. Furthermore, chiral assembly arrays with programmable pattern can also be flexibly fabricated by controlling the 3D piezoelectric displacement platform (PI E545) movement and the shutter ON/OFF. As a demonstration, a “Tai Chi” pattern in which the left-handed and right-handed chiral microstructures are pre-designed is prepared (Figure 4b). The SEM and fluorescence images show that the eyes of “Tai Chi” array are

respectively arranged with left-handed (marked with a red circle) and right-handed (marked with a green circle) assemblies.

In addition to adjusting the chirality of microstructure, chiral assemblies with different petal numbers can also be flexibly fabricated by controlling the number of vortex beams involved in the interference. To obtain evenly distributed CDVB intensity, the centers of the interfering vortex beams should be arranged as a regular polygon. The CDVB light field and the corresponding microstructures from 3-vortex interference to 6-vortex interference are shown in Figure 4c, respectively. The holograms (first row) and simulated intensity distribution (second row) of the CDVB with increasing interfering vortex beams are sequentially generated. Chiral assemblies with the corresponding petal numbers are obtained. Since the stability of the chiral microstructure is important, and the triangle is the simplest and most stable shape, here we choose the three-vortex interference to fabricate the pyramid-like microstructure. The top-view (third row) and 45° tilted (fourth row) SEM images of chiral assemblies from 3 to 6 petals confirm that the morphologies of the prepared chiral assemblies are diverse and can be flexibly adjusted. It is worth noting that this approach can improve the fabrication efficiency by 102 times and prepare the chiral microstructure with surface smoothness on the order of 10 nm as shown in Section 6 of supporting information, which means that the large area and mass production can be realized by controlling a large-stroke motion platform and SLM.

2.5. Vortex Dichroism Response on Chiral Assemblies

It has been proved in many studies that the optical response can be significantly enhanced by 3D chiral microstructures, which has been applied in various applications including broadband

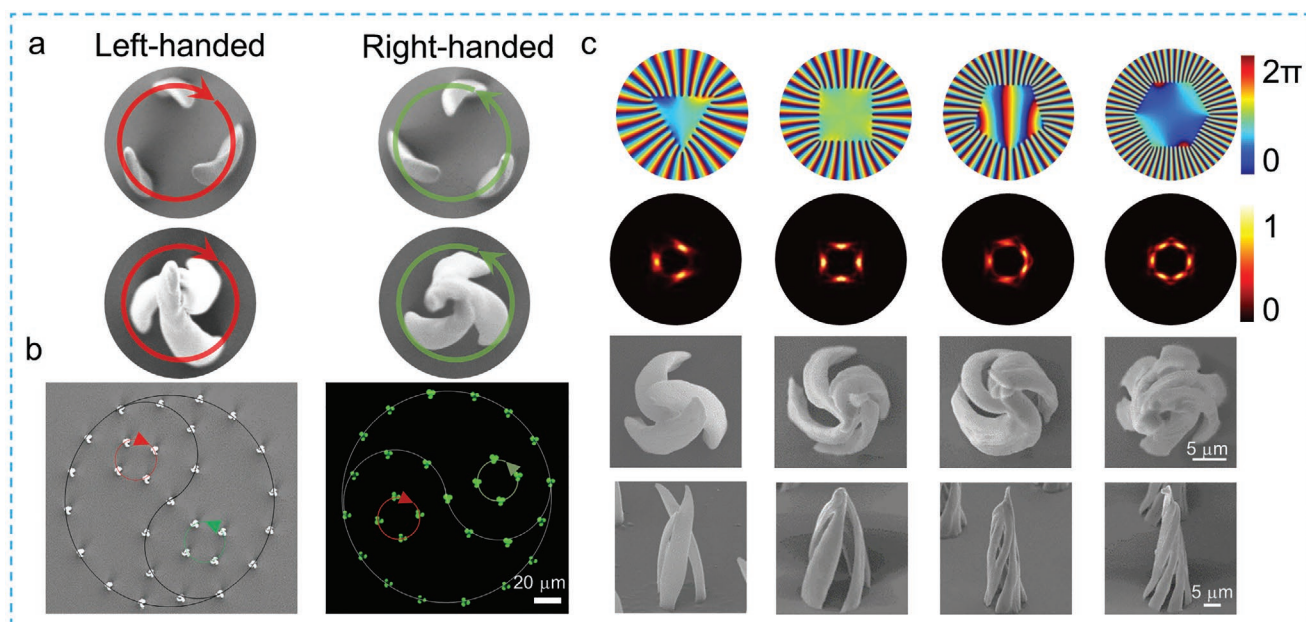


Figure 4. The 3D chiral microstructures with various morphologies. a) Top view SEM images of the left-handed/right-handed un-assembled and assembled chiral microstructures. b) Left- handed and right- handed chiral microstructure are arranged in the pattern of Tai Chi. c) SEM images of chiral assemblies with different petal numbers (third and fourth rows) and their corresponding holograms (first row) and light intensity distributions (second row).

circular polarizers and near-infrared optical rotation devices.^[2,17] The prepared assemblies in this work have chiral spatial morphologies, which can produce a strong optical response to OAM beams.^[18] Light carrying the OAM has been proven to possess the ability to distinguish chiral enantiomers. In analogous to circular dichroism (CD) detection, the differential reflection of the incident vortex beams with opposite OAM modes on chiral microstructure can be observed, which is defined as vortex dichroism (VD). This OAM-dependent VD phenomenon has essential difference with conventional CD, and the comparison between the CD and VD on the chiral assembly is shown in Figure S24 in the Supporting Information. In the simulation, the wavelength-dependent CD has extremely weak signal (<0.3%) in the range of 600 nm to 1000 nm (Figure S25, Supporting Information), while the OAM-dependent VD is significant (~20%) for the chiral assemblies (Figure S26, Supporting Information). The results show the advantageous of the VD detection in the micro-sized chiral optics, and demonstrate the prospect of our chiral 3D microstructure as a VD detection platform. In the experiment, the measurement schematic and results of VD on chiral assemblies are shown in **Figure 5**. Take the detection of left-handed assembly as an example, vortex beams carrying the opposite OAM are irradiated vertically on an assembly selected from the array (Figure 5a). Firstly, the OAM beam is focused on the chiral microstructures by the system shown in Figure S27 in the Supporting Information. Then the reflected light is collected by a camera and analyzed by the commercial software MATLAB. The calculation processes and original reflection data are shown in Figures S28 and S29 in the Supporting Information. Similar to the CD evaluation, the VD can be defined as

$$VD = 2 \times \frac{I_{+l} - I_{-l}}{I_{+l} + I_{-l}} \times 100\% \quad (10)$$

where I_{+l} and I_{-l} are the reflection intensity under the illumination of optical vortices with topological charge $+l$ (left-handed helical wavefront, LHW) and $-l$ (right-handed helical wavefront, RHW). In the detection process, the OAM beams with a constant wavelength and a definite topological number

interacts with the chiral beams, causing the change of discrete OAM spectrum and the generation of VD. The detailed discussion about the relationship between the incident beam and reflected beam can be seen in the Section 9 of supporting information. This method can robustly generate chiroptical properties on microstructures with varying geometric features and plays an important role in the chiral detection. For example, VD detection can be combined with metasurfaces with nanostructures for generating and detecting vortex beams with different topological charges, which will have promising future in optical communications and optical sensing.^[19] And the detection process of the right-handed assembly is the same as that of a left-handed one, as shown in Figure 5b.

Measured VD spectrums of assemblies with opposite chirality and glass substrate are shown in Figure 5c. The VD spectral lines of the opposite chiral assemblies are approximately symmetrical with respect to the substrate's spectral line. The symmetry error of the signal is caused by factors such as uneven energy distribution of the probe beam and imperfect structural space symmetry. In terms of the left-handed assembly, the VD signals are positive in the coupling area ($||l| < 55$), and there is a strong peak at $||l| = 33$ due to the optimal coupling state in the interaction between vortex beams and the assembly. Therefore, it may be predicted that this regular VD response also makes the chiral assemblies feasible probes for distinguishing the symbolic and topological charges of monochromatic vortex beams. Furthermore, the scattering intensity on the substrate decreases as the absolute value of the topological charge increases (Figure S29, Supporting Information), due to the change of beam coverage. However, this impact is naturally eliminated by the formula $VD = 2 \times \frac{I_{+l} - I_{-l}}{I_{+l} + I_{-l}} \times 100\%$ because

the VD is calculated by the ratio of the absolute reflection difference and the average value of I_{+l} and I_{-l} , which is similar with the circular dichroism characterization. The OAM modes of the incident and reflected beams were also analyzed for further revealing the modulation effect of the chiral structure on the vortex beam (Figure S30, Supporting Information). Besides, because the chiral microstructure should be submerged in a solution for sensing and measuring purposes in some

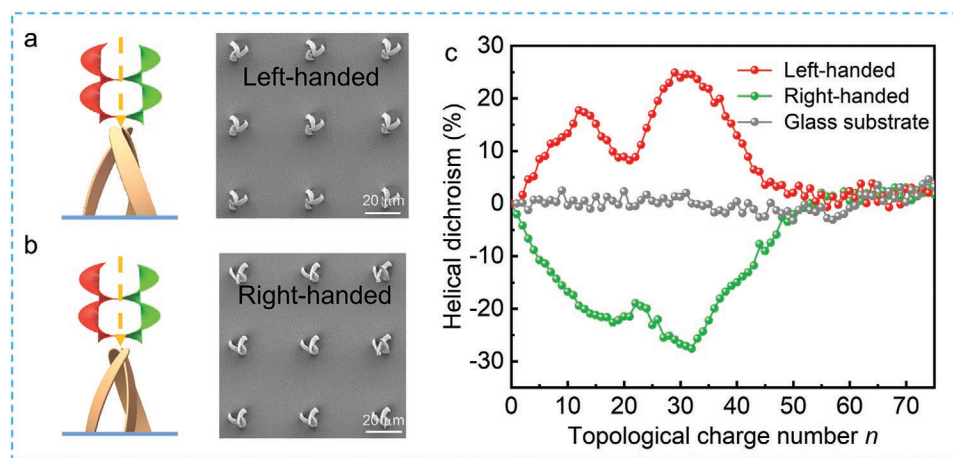


Figure 5. Vortex dichroism response on 3D chiral assemblies. a,b) Schematic diagrams of the OAM response and the SEM images of the chiral microstructures used in the experiment. c) Measured VD spectrums of assemblies with opposite chirality and glass substrate.

situations, the stability of the microstructure is important. For evaluating the stability of the prepared 3D chiral microstructures, we submerged and dried the assembled microstructures in acetone, ethanol, n-propanol, isopropanol, water, and phosphate buffered saline (PBS) in turn. As shown in Figures S31 and S32 in the Supporting Information, benefiting from the capillary-force-assisted assembly, the pyramid-shaped constructed chiral microstructures exhibited good stability in the test, and did not distort or collapse after repeated drying.

2.6. Preparation and Manipulation of Bionic Chiral Microrobots with Programmable Heads

The microrobots, also called microscale machines, are functional device whose size is usually less than $1\text{ mm} \times 1\text{ mm}$.

They can perform various tasks such as micromanipulation, drug delivery and non-invasive surgery.^[20] For example, The helix microrobots,^[21] as a classical magnetic microrobots, can move in a specified direction under the control of an external magnetic field, and has been widely investigated in the field including targeted drug/gene delivery,^[22] cell Manipulation,^[23] and sensing.^[24] Here, as a demonstration of concept, the potential of the 3D chiral microstructures as artificial microrobots is discussed. Firstly, mass production of the 3D chiral assemblies can be easily and efficiently obtained by capillary-assisted assembly. After the assembling, the photoresist is dropped onto the microstructures again, and any programmable structure can be re-written on the top of the chiral assemblies as a “functional head” (Figure 6a). Several kinds of 3D chiral microrobots with cylindrical (Figure 6b), cone-shaped (Figure 6c) and phage-shaped (Figure 6d) heads are designed and fabricated as

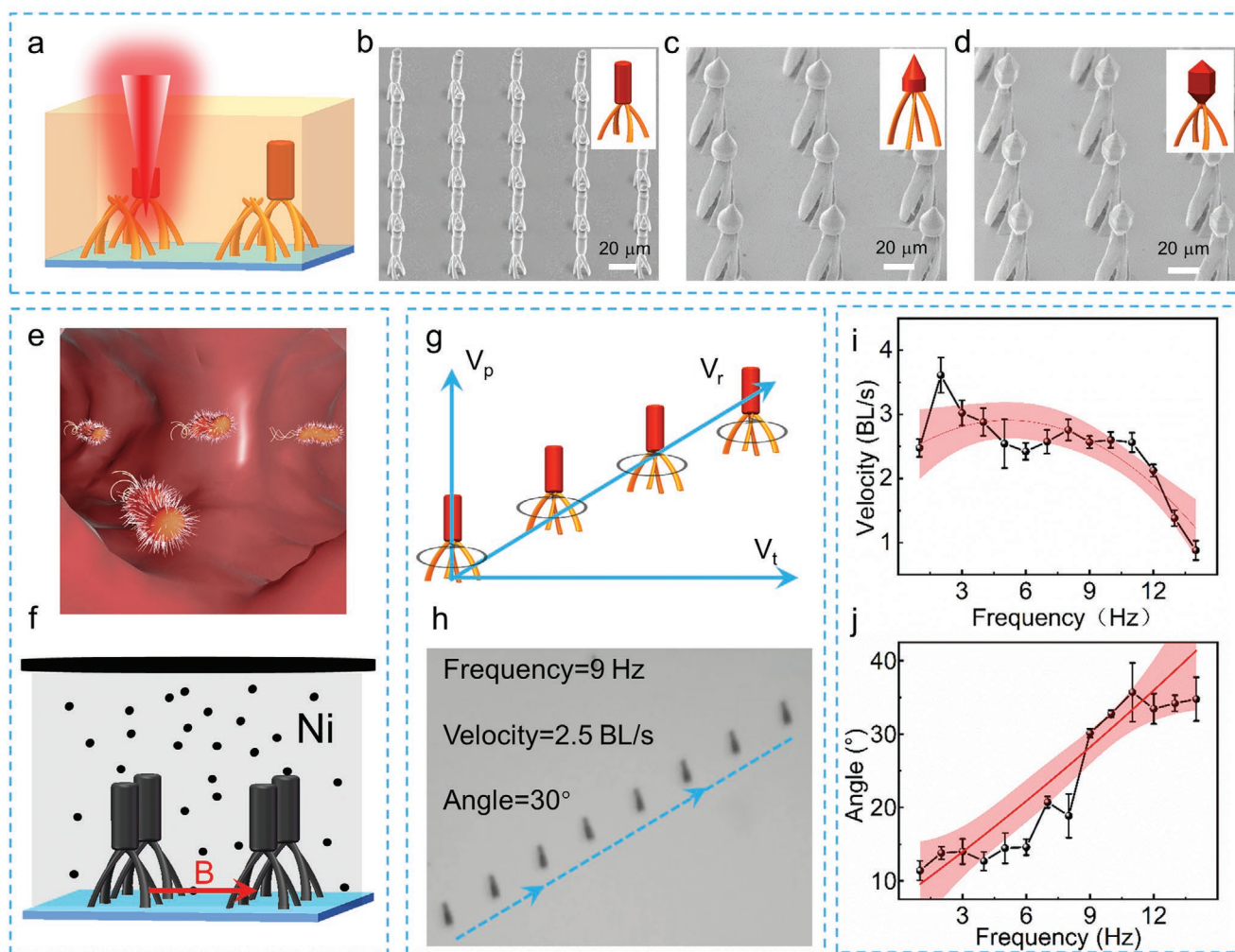


Figure 6. Preparation and manipulation of bionic chiral microrobots. a) Preparation process of the microrobots with programmable functional head. The assembled chiral microstructure can act as the body and any shaped functional head such as b) cylindrical, c) cone-shaped, and d) phage-shaped can be re-fabricated onto it. e) Schematic diagram of driveable bionic micro-robot. f) The chiral microstructure with functional head needs to be deposited by 200 nm thickness Ni. The magnetic axis needs to be initialized to the horizontal direction by applying an external magnetic field. g) The resultant speed of the micro robot is the vector addition of the translational speed along the horizontal direction and the advancing speed along the vertical direction. h) The moving process of the microrobots under the driving frequency of 9 Hz. i, j) The moving velocity and moving angle of the microrobots under different driving frequency. The curve formulas are $y = 2.3 + 0.22x - 0.02x^2$ and $y = 7.4 + 2.1x + 0.02x^2$ respectively. The 95% confidence interval is shown by the red area.

a demonstration. It can be prospected that different functional heads can be designed to endue 3D chiral microrobots various functions. For example, the cylindrical head may be used for medicine storage, and the tapered head may be used for blood vessel drilling. Then, for making the 3D chiral microrobots rotate and move forward under the action of an external magnetic field (Figure 6e), a layer of 200 nm thick Nickel is deposited on the outer surface of the microrobots with the thermal evaporation system (Figure 6f). After the evaporation, the whole sample is placed between two permanent magnets for 24 hours to re-magnetize the sample and determine the magnetic axis distribution along the short axis of microrobots (Figure S33, Supporting Information). Finally, the 3D chiral microrobots are released into the water by a microneedle and driven by a rotating magnetic field.

During the moving process, the Helmholtz coils are used to generate rotating magnetic fields (Figure S34, Supporting Information), and the vector velocity of the 3D chiral micro-robot is the superposition of two velocity components, which are the forward velocity V_p and the drift velocity V_t generating from the liquid pushing and self-rotation, respectively (Figure 6g). For example, when the frequency of the external rotation magnetic field is 9 Hz, the velocity of 3D chiral microrobots is 2.5 body lengths per second, and the moving direction is 30 degrees relative to horizontal (Figure 6h). Besides, the microrobots can react to the changes of the alternating magnetic field and make different motion responses (Figure 6i,j). It is worth noting that the total velocity of the microrobots first increases as the frequency of the magnetic field increases, and then decreases after reaching the out-of-step frequency at 11 Hz. Finally, the speed drops to 0 at 15 Hz. Compared with the complex changes of the forward velocity, the moving angle simply increases with the increase of the frequency, which means that a larger magnetic field frequency can result in a smaller lateral drift of the microrobots (Figure S35, Supporting Information). In this demonstration, it can be considered that multi-petal microrobots have the best swimming performance when the magnetic field frequency is 10 Hz by considering the moving velocity and angle, which shows that this method provides a solution for the rapid preparation of biomimetic magnetic microrobots.

3. Conclusion

In this paper, a hybrid strategy for efficient preparation of the 3D chiral microstructures by combing the self-assembly and SATPP is proposed. Multiple parallel vortex beams interference is proposed for generating a 3D chiral femtosecond laser beam. With the aid of the SLM-assisted TPP system, subunits can be fabricated efficiently by the CDVB single exposure. The 3D chiral microstructures are assembled and regulated by capillary force. Benefiting from the flexibility of this strategy, the parameters of the discrete or assembled chiral microstructures can be regulated flexibly. During the preparation process, a 3D chiral microstructure can be fabricated within 0.5 s, which improves the fabrication efficiency by 102 times and provides the possibility for the large-scale production. The prepared chiral microstructures exhibit strong vortex dichroism when excited by the

light carrying orbital angular momentums. Besides, the 3D chiral microstructures can be used to prepare the functional microrobots. The moving speed and the moving direction can be adjusted by the magnetic field. The hybrid strategy proposed in this work can prepare 3D chiral microstructures efficiently, flexibly, and economically, which have potential applications in the field of micro/nano robots, optical sensing, advanced functional devices, and etc.

4. Experimental Section

Femtosecond Laser Two-Photon Polymerization: The femtosecond laser used in this work is a mode-locked titanium-sapphire oscillator made by Coherent Inc. The laser source has a center wavelength of 800 nm, pulse width 75 femtosecond, and a repetition rate 80 MHz. A pure phase reflective liquid crystal silicon-based spatial light modulator is used (Pluto NIR-2).

Holograms Generation and Optical Beams Simulations: The resolution of the spatial light modulator is 1920×1080 , and the pixel pitch is $8 \mu\text{m}$. During the exposing process, an 8-bit format grayscale image with 256 tunable grayscales is used to modulate the laser wavefront. The hologram of CDVB is calculated by the commercial software MATLAB 2018a. All the holograms are designed as 1080×1080 matrixes. The incident beam can be writtend as $E(x,y) = A(x,y)\exp[i\varphi(x,y)]$, and the phase $\varphi(x,y)$ can be calculated by superposing multiple vortex wavefront as shown in Formula 1. The focused light field simulation is executed on the mathematical software Matlab (2018a). According to the Debye diffraction integration algorithm, the focused light field on the focal plane can be obtained.

VD Simulations: The reflection numerical simulations were performed by a finite-difference time-domain-based software (Lumerical FDTD Solutions, Inc.). In the simulation, the model of the chiral structure is created by the FDTD script function, which is consistent with the actual processing structure, and the refractive index of the chiral structure was set to be 1.51. Perfectly matched layer boundaries were applied for the X, Y, and Z directions, and the minimum mesh step was set to be 50 nm. For the VD simulation, the incident light source is set to be linearly polarized vortex light with varying topological charge number at a fixed wavelength of 800 nm. While for the CD simulation, the incident light source is left-handed or right-handed circularly polarized light with continuously changing wavelengths from 600 to 1000 nm

Sample Preparation: The photoresist used in this work was a hybrid organic-inorganic material (SZ2080) bought from IESL-FORTH. Before fabrication, the 15 μL photoresist was dropped on a 20 mm \times 20 mm cleaned glass slide and heated at 100 $^\circ\text{C}$ for 60 min. After the fabrication, the whole sample was immersed in-propanol acetone for 30 minutes until the unprocessed area was removed. After that, the sample was taken out and dried in the air for assembling the sub-units into a 3D chiral microstructure.

Characterization: The SEM images were taken by a scanning electron microscope (EVO18, ZEISS), and the optical images are taken by an optical microscope (DMI3000B, Leica). The VD spectrum was measured by the CCD (WV-BP334, Panasonic) and calculated by MATLAB 2018b. During the measurement, the optical vortex was generated by the SLM and aligned to the center of the microstructure. The movement control was achieved by a nano positioning stage (E545, Physik Instrumente) with nanometer resolution and 200 μm movement range.

Supporting Information

Supporting Information is available from the Wiley Online Library or from the author.

Acknowledgements

D.P. and S.L. contributed equally to this work. This work was supported by the National Natural Science Foundation of China (Nos. 61927814, 91963127, 51875544, 51805509, 52075516, 52105583), Major Scientific and Technological Projects in Anhui Province (201903a05020005), and the Fundamental Research Funds for the Central Universities (WK5290000002, WK2090000016, WK2090050048). The authors acknowledge the Experimental Center of Engineering and Material Sciences at USTC for the fabrication and measuring of samples. This work was partly carried out at the USTC Center for Micro and Nanoscale Research and Fabrication.

Conflict of Interest

The authors declare no conflict of interest.

Data Availability Statement

Research data are not shared.

Keywords

3D chiral microstructures, bionic microrobots, self-assembly, two-photo polymerization, vortex beams

Received: July 16, 2021

Revised: September 24, 2021

Published online: October 12, 2021

- [1] K. Tsuji, S. C. Müller, Spirals and Vortices: In Culture, *Nature, and Science*, Springer, Berlin **2019**.
- [2] M. Hentschel, M. Schäferling, X. Duan, H. Giessen, N. Liu, *Sci. Adv.* **2017**, *3*, 1602735.
- [3] a) K. Dietrich, C. Menzel, D. Lehr, O. Puffky, U. Hübner, T. Pertsch, A. Tünnermann, E. B. Kley, *Appl. Phys. Lett.* **2014**, *104*, 193107; b) M. Decker, R. Zhao, C. M. Soukoulis, S. Linden, M. Wegener, *Opt. Lett.* **2010**, *35*, 1593; c) M. L. Tseng, Z. H. Lin, H. Y. Kuo, T. T. Huang, Y. T. Huang, T. L. Chung, C. H. Chu, J. S. Huang, D. P. Tsai, *Adv. Opt. Mater.* **2019**, *7*, 1900617.
- [4] a) M. D. Turner, M. Saba, Q. Zhang, B. P. Cumming, G. E. Schröder-Turk, M. Gu, *Nat. Photonics* **2013**, *7*, 801; b) S. Bianchi, G. Vizsnyiczai, S. Ferretti, C. Maggi, R. Di Leonardo, *Nat. Commun.* **2018**, *9*, 4476; c) D. Wu, L. G. Niu, S. Z. Wu, J. Xu, K. Midorikawa, K. Sugioka, *Lab Chip* **2015**, *15*, 1515; d) A. Marino, O. Tricinci, M. Battaglini, C. Filippeschi, V. Mattoli, E. Sinibaldi, G. Ciofani, *Small* **2018**, *14*, 1702959.
- [5] Z. Lao, N. Xia, S. Wang, T. Xu, X. Wu, L. Zhang, *Micromachines* **2021**, *12*, 465.
- [6] a) R. Li, D. Jin, D. Pan, S. Ji, C. Xin, G. Liu, S. Fan, H. Wu, J. Li, Y. Hu, D. Wu, L. Zhang, J. Chu, *ACS Nano* **2020**, *14*, 5233; b) B. Xu, S. Ji, D. Pan, W. Hu, S. Zhu, Y. Hu, J. Li, D. Wu, J. Chu, K. Sugioka, *Opt. Lett.* **2020**, *45*, 1071; c) S. Y. Ji, R. Li, Z. Cai, D. Pan, L. Yang, Y. L. Hu, J. W. Li, D. Wu, J. R. Chu, *Opt. Lett.* **2019**, *44*, 5073; d) D. Pan, Z. Cai, S. Y. Ji, S. Y. Fan, P. R. Wang, Z. X. Lao, L. Yang, J. C. Ni, C. W. Wang, J. W. Li, Y. L. Hu, D. Wu, S. C. Chen, J. R. Chu, *ACS Appl. Mater. Interfaces* **2018**, *10*, 36369; e) C. Wang, L. Yang, Y. Hu, S. Rao, Y. Wang, D. Pan, S. Ji, C. Zhang, Y. Su, W. Zhu, J. Li, D. Wu, J. Chu, *ACS Nano* **2019**, *13*, 4667; f) D. Pan, S. Liu, S. Ji, Z. Cai, J. Li, Y. Hou, W. Zhang, S. Fan, R. Li, Y. Hu, W. Zhu, D. Wu, J. Chu, *Opt. Lett.* **2020**, *45*, 897; g) D. Pan, B. Xu, S. Liu, J. Li, Y. Hu, D. Wu, J. Chu, *Opt. Lett.* **2020**, *45*, 2584; h) S. Ji, L. Yang, Y. Hu, J. Ni, W. Du, J. Li, G. Zhao, D. Wu, J. Chu, *Small* **2017**, *13*, 1701190.
- [7] D. Yang, L. Liu, Q. Gong, Y. Li, *Macromol. Rapid Commun.* **2019**, *40*, 1900041.
- [8] a) C. Cummins, R. Lundy, J. J. Walsh, V. Ponsinet, G. Fleury, M. A. Morris, *Nano Today* **2020**, *35*, 100936; b) A. Neophytou, V. N. Manoharan, D. Chakrabarti, *ACS Nano* **2021**, *15*, 2668.
- [9] D. Zerrouki, J. Baudry, D. Pine, P. Chaikin, J. J. N. Bibette, **2008**, *455*, 380.
- [10] M. Y. B. Zion, X. He, C. C. Maass, R. Sha, N. C. Seeman, P. M. J. S. Chaikin, **2017**, *358*, 633.
- [11] a) Y. Hu, Z. Lao, B. P. Cumming, D. Wu, J. Li, H. Liang, J. Chu, W. Huang, M. Gu, *Proc. Natl. Acad. Sci.* **2015**, *112*, 6876; b) Z. X. Lao, Y. L. Hu, D. Pan, R. Y. Wang, C. C. Zhang, J. C. Ni, B. Xu, J. W. Li, D. Wu, J. R. Chu, *Small* **2017**, *13*, 1603957; c) Z. Lao, D. Pan, H. Yuan, J. Ni, S. Ji, W. Zhu, Y. Hu, J. Li, D. Wu, J. Chu, *ACS Nano* **2018**, *12*, 10142; d) H. Duan, H. Hu, K. Kumar, Z. Shen, J. K. Yang, *ACS Nano* **2011**, *5*, 7593.
- [12] B. Pokroy, S. H. Kang, L. Mahadevan, J. Aizenberg, *Sci.* **2009**, *323*, 237.
- [13] C. W. Qiu, Y. Yang, *Sci.* **2017**, *357*, 645.
- [14] a) H. Li, G. M. Wang, G. Hu, T. Cai, C. W. Qiu, H. X. Xu, *Adv. Opt. Mater.* **2020**, *8*, 2000129; b) A. M. Yao, M. J. Padgett, *Adv. Opt. Photonics* **2011**, *3*, 161; c) Y. Yang, L. Wu, Y. Liu, D. Xie, Z. Jin, J. Li, G. Hu, C. W. Qiu, *Nano Lett.* **2020**, *20*, 6774.
- [15] A. M. Amaral, E. L. Falcao-Filho, C. B. de Araujo, *Opt. Lett.* **2013**, *38*, 1579.
- [16] P. Delrot, D. Loterie, D. Psaltis, C. Moser, *Opt. Express* **2018**, *26*, 1766.
- [17] a) J. K. Gansel, M. Thiel, M. S. Rill, M. Decker, K. Bade, V. Saile, G. von Freymann, S. Linden, M. Wegener, *Science* **2009**, *325*, 1513; b) Z. Liu, H. Du, J. Li, L. Lu, Z. Y. Li, N. X. Fang, *Sci. Adv.* **2018**, *4*, eaat4436.
- [18] a) J. Ni, S. Liu, D. Wu, Z. Lao, Z. Wang, K. Huang, S. Ji, J. Li, Z. Huang, Q. Xiong, Y. Hu, J. Chu, C. W. Qiu, *Proc. Natl. Acad. Sci. USA* **2021**, *118*, 2020055118; b) J. Ni, S. Liu, G. Hu, Y. Hu, Z. Lao, J. Li, Q. Zhang, D. Wu, S. Dong, J. Chu, C. W. Qiu, *ACS Nano* **2021**, *15*, 2893; c) J. Ni, Y. Hu, S. Liu, Z. Lao, S. Ji, D. Pan, C. Zhang, B. Xu, J. Li, D. Wu, J. Chu, *Opt. Lett.* **2021**, *46*, 1401.
- [19] a) M. Q. Mehmood, S. Mei, S. Hussain, K. Huang, S. Y. Siew, L. Zhang, T. Zhang, X. Ling, H. Liu, J. Teng, A. Danner, S. Zhang, C. W. Qiu, *Adv. Mater.* **2016**, *28*, 2533; b) Y. Bao, J. Ni, C. W. Qiu, *Adv. Mater.* **2020**, *32*, 1905659.
- [20] L. Tan, A. C. Davis, D. J. J. A. F. M. Cappelleri, **2021**, *31*, 2007125.
- [21] C. Xin, L. Yang, J. Li, Y. Hu, D. Qian, S. Fan, K. Hu, Z. Cai, H. Wu, D. Wang, D. Wu, J. Chu, *Adv. Mater.* **2019**, *31*, 1808226.
- [22] a) F. M. Qiu, S. Fujita, R. Mhanna, L. Zhang, B. R. Simona, B. J. Nelson, *Adv. Funct. Mater.* **2015**, *25*, 1666; b) H. Ceylan, I. C. Yasa, O. Yasa, A. F. Tabak, J. Giltinan, M. Sitti, *ACS Nano* **2019**, *13*, 3353.
- [23] a) X.-Z. Chen, J.-H. Liu, M. Dong, L. Müller, G. Chatzipirpiridis, C. Hu, A. Terzopoulou, H. Torlacik, X. Wang, F. Mushtaq, J. Puigmartí-Luis, Q.-D. Shen, B. J. Nelson, S. Pané, *Mater. Horiz.* **2019**, *6*, 1512; b) S. Jeon, S. Kim, S. Ha, S. Lee, E. Kim, S. Y. Kim, S. H. Park, J. H. Jeon, S. W. Kim, C. Moon, B. J. Nelson, J. Y. Kim, S. W. Yu, H. Choi, *Sci. Rob.* **2019**, *4*, eaav4317.
- [24] A. Ghosh, D. Dasgupta, M. Pal, K. I. Morozov, A. M. Leshansky, A. Ghosh, *Adv. Funct. Mater.* **2018**, *28*, 1705687.